

# Intelligent Remote Sensing Image Quality Inspection System

Yijiong Yu <sup>1,2</sup>, Tao Wang <sup>2,\*</sup>, Kang Ran <sup>2</sup>, Chang Li <sup>2</sup> and Hao Wu <sup>2</sup>

<sup>1</sup> Department of Electronic Engineering, Tsinghua University; yuyj22@mails.tsinghua.edu.cn

<sup>2</sup> Guizhou Surveying and Mapping Product Quality Supervision and Inspection Station, Guiyang 550000, China

\* Correspondence: wangt.07b@igsnr.ac.cn; Tel.: +86-136-0855-3930

**Abstract:** Quality inspection is a necessary task before putting any remote sensing image into practical application. However, traditional manual inspection methods suffer from low efficiency. Hence, we propose a novel two-step intelligent system for remote sensing image quality inspection that combines multiple models, which first performs image classification and then employs the most appropriate methods to localize various forms of quality problems in the image. Results demonstrate that the proposed method exhibits excellent performance and efficiency in remote sensing image quality inspection, surpassing the performance of those one-step methods. Furthermore, we conduct an initial exploration of the feasibility and potential of applying multimodal models to remote sensing image quality inspection.

**Keywords:** remote sensing image quality inspection; deep learning; image classification; semantic segmentation; multimodal models

## 1. Introduction

In recent years, rapid advancements in remote sensing technology have enabled the acquisition of large amounts of high-resolution remote sensing imagery, which has been widely applied in geological exploration, environmental monitoring, agriculture, and other fields. However, the raw remote sensing images often suffer from various quality issues such as cloud cover, shadow, and blur, which significantly affect their usability and interpretability. Figure 1 illustrates ten common error types in remote sensing image quality inspection. Note that the remote sensing images in this paper default to RGB format without invisible spectrums.

Automated and intelligent research in the field of remote sensing image quality inspection has been scarce until now. Almost all existing works heavily rely on manual inspection by professional technicians, which, although ensures reliable results, lacks efficiency. Over the past decade, some automated detection methods have been proposed and achieved good detection results, such as object-based cloud detection methods [1], but such methods can only target specific objects. Therefore, it is of great significance to develop an efficient and accurate automated method for remote sensing image quality inspection.

The primary goal of remote sensing image quality inspection is to identify and locate the areas that do not meet the quality standards, and calculate their respective areas to evaluate the quality score of the entire remote sensing image. This can be easily related to the image segmentation task.

Image segmentation is a time-honored subject, in which the most commonly used method is threshold-based algorithms. In addition, there are clustering methods, edge-based methods, region-based methods, graph-based methods [2]. Deep learning-based methods perform segmentation by learning samples without manually designing rules, and are currently the most powerful.

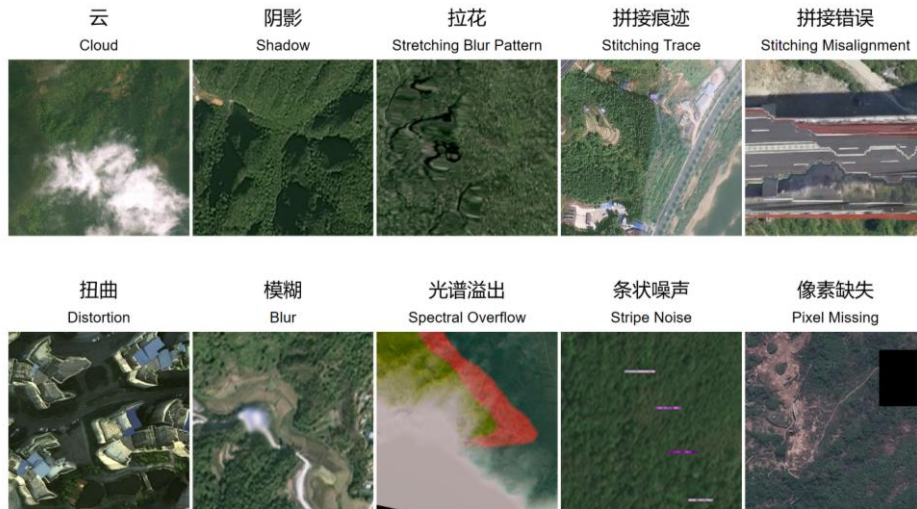


**Figure 1.** Example images of 10 error types and corresponding Chinese and English names.

Deep learning techniques have made remarkable achievements in the field of computer vision, demonstrating powerful capabilities in image classification, object detection, semantic segmentation, and other tasks, which greatly promotes the development of remote sensing image processing field. In the field of image classification, the representative CNN-based [3] models ones are AlexNet [4], ResNet [5], DenseNet [6], MobileNet [7], etc. and in the image segmentation field, they are FCN [8], Unet [9], etc. Transformer-based [10] models, such as Swin [11] for image classification and Segformer [12] for semantic segmentation, are more advanced, and are gradually replacing the traditional CNN models.

Semantic segmentation is a task that assigns every pixel a class label of its corresponding image object and remote sensing image quality inspection appears to be a straightforward semantic segmentation problem, however, purely applying one semantic segmentation model would lead to a dilemma caused by the characteristics of the task. In the remote sensing images to be inspected, more than 80% of the area typically belongs to the qualified region. In other words, if all regions of remote sensing images are used to train a semantic segmentation model without selection, the positive and negative samples will be highly imbalanced. The number of negative samples (images containing only qualified regions) will be much greater than positive samples, resulting in a low recall score of the trained model. Even the use of weighted loss cannot fully address this issue. On the other hand, using only positive samples (images containing areas of errors) for training leads to low precision. In summary, the sample distribution in the dataset is highly inconsistent with the reality, making it difficult to obtain a model with both high precision and recall.

Furthermore, not all error types are suitable for semantic segmentation. Some error regions have very tiny areas, making them difficult to detect using semantic segmentation models. Specific image processing techniques based on rules are still suitable for detecting such types of errors.

To address the above problems, we propose an intelligent two-step detection system. During detection, an image classification model is first used to determine the presence of these 10 error types in each block. Subsequently, based on the distinctive morphological characteristics of different error types and their follow-up handling in practical work, we categorize 10 error types into 3 major classes and design a specific method to detect each, which will be introduced in detail in section 3. The experimental results confirm the superiority of our two-step approach compared to previous methods.

In summary, the main contributions of this paper are as follows:

1. We annotated the image segmentation dataset for remote sensing image quality inspection and, to our knowledge, this is the first publicly available dataset in this field.

2. We perform a specific analysis for each error type, categorize them, and design the most suitable detection method for each major class.
3. We conducted comparative experiments on the effects of various existing image processing methods, image classification models, semantic segmentation models and multi-modal models in the remote sensing image quality inspection task, and selected the optimal model for practical work according to the experimental results.
4. We propose a method to integrate two models to substantially reduce the misdetection rate, and accordingly construct the two-step detection system, whose overall process is shown in Figure 2.

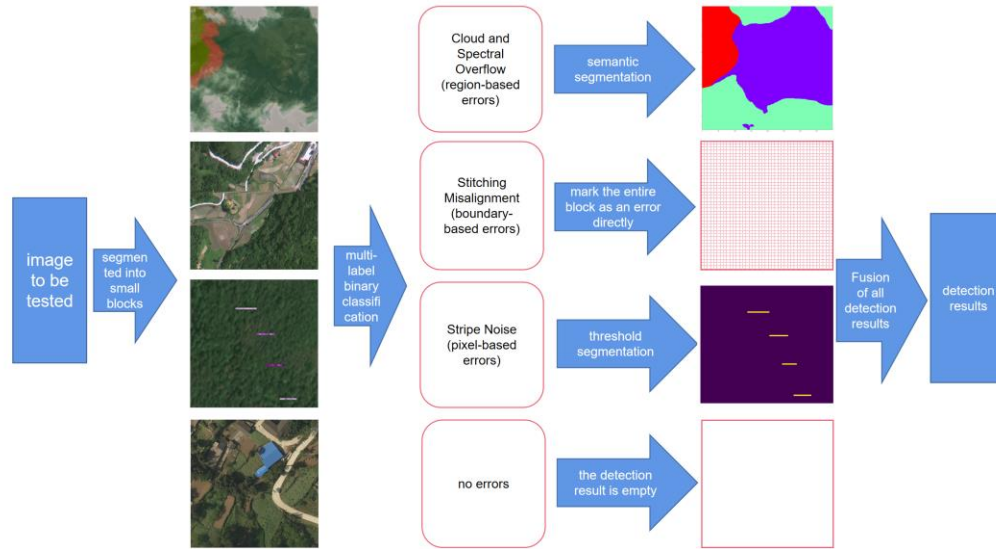


**Figure 2.** Overall process of the two-step detection system

Although the system that use multiple models and image processing methods have achieved good results, its procedures are somehow complex and only applicable to specific problems. Completing all quality inspection tasks through a single universal model like GPT-4 [13] will be much more convenient and higher-level intelligent. Based on this intention, we explores the role of multimodal models such as the BLIP model [14] and VisualGLM model [15] in remote sensing image quality inspection. These multimodal models not only serve as image classifiers but also a Chatbot, which means they can provide more comprehensive, detailed, and customizable descriptions about the regions of errors in the remote sensing image, such as areas, locations, colors and shapes, to some extent replacing image classification models and segmentation models.

## 2. Data

### 2.1. Data Source

The data used in this study is obtained from the Guizhou Surveying and Mapping Product Quality Supervision and Inspection Station and all remote sensing images are taken from Guizhou Province, China, whose climate is cloudy and foggy, and the main terrain is mountainous. The original image is in RGB format, with file sizes usually ranging from 300M to 10G and image widths typically greater than 3000 pixels. Each remote sensing image has been manually annotated by professional technicians to identify the regions of the 10 types of errors. The annotated regions include information such as error type, area, and penalty score. The annotation information for each image is stored in a shapefile (.shp) format, where each error region is represented as a polygon, in which each point has latitude and longitude coordinate.

### 2.2. Dataset Creation

Based on the polygon information recorded in the shapefile, and the corresponding remote sensing images in RGB, the detection results are generated using the "draw\_polygon"

function of scikit-image python package, creating masks that correspond to the inspection results. The mask is a single-channel image where pixels with a value of 0 represent qualified regions (also called background), while other pixel values represent different error types. A pixel value of 255 is used to indicate areas that can be ignored, typically representing the black-filled areas outside the range of the remote sensing image. The mapping between pixel values and error types is shown in Table 1.

**Table 1.** Mappings between pixel value and category.

pixel value	label
0	Background
1	Cloud
2	Shadow
3	Stretching Blur Pattern
4	Blur
5	Spectral Overflow
6	Distortion
7	Stitching Trace
8	Stitching Misalignment
9	Stripe Noise
10	Pixel Missing
255	(ignored)

Because the original image size is very huge, to fit the input size of deep learning models, the remote sensing images and their masks are divided into smaller blocks of size 512x512 and 1024x1024. Each block in the remote sensing image corresponds to a block in the mask, creating a semantic segmentation dataset containing image and mask pairs. Furthermore, using the information in the masks, the dataset is further expanded to include the set of error types present in the mask. Additionally, textual descriptions of the images are generated based on certain rules, as outlined in Table B1. The final dataset consists of four columns: image, mask, label set, and textual description, with the data formats being a RGB image, a single-channel mask, a list of label ids, and string respectively. The textual descriptions are all in Chinese.

The dataset contains 2855 realistic remote sensing images with error regions. To make the distribution of the dataset closer to the sample distribution in real-world environments, 1027 qualified remote sensing images are added as negative samples. Subsequently, the dataset is randomly split into training and testing sets in a 9:1 ratio, while ensuring that the proportions of different image types remain balanced in both sets. The final training set contains 3492 samples, and the testing set contains 390 samples.

### 2.3. Creation of Image-based Question-Answer Dataset

The training of a multimodal large model requires the creation of image-based question-answer pairs. Since a single question-answer pair may not fully describe the image information, multiple question-answer pairs are needed. While manually crafting question-answer pairs yields higher quality, it is a costly process. In this study, the question-answer pairs are generated based on the information extracted from the masks using specific rules, which are provided in Table B1, Table B2 and Table B3.

The language used for both the questions and answers is Chinese. If an answer starts with "否" (no), it is considered a negative sample. Having too many negative samples can adversely affect the model's performance, so 20% of the negative samples are randomly retained. The resulting question-answer dataset comprises 10,457 samples for the training set and 1,176 samples for the test dataset.

### 2.4. Data Augmentation

The occurrence frequencies of quality issues in remote sensing images are highly imbalanced. Figure 3 shows the number of samples containing each error type, revealing that certain categories such as Stitching Trace and Spectral Overflow occur much less frequently. As a consequence, the accuracy of classification for these categories will be generally lower.

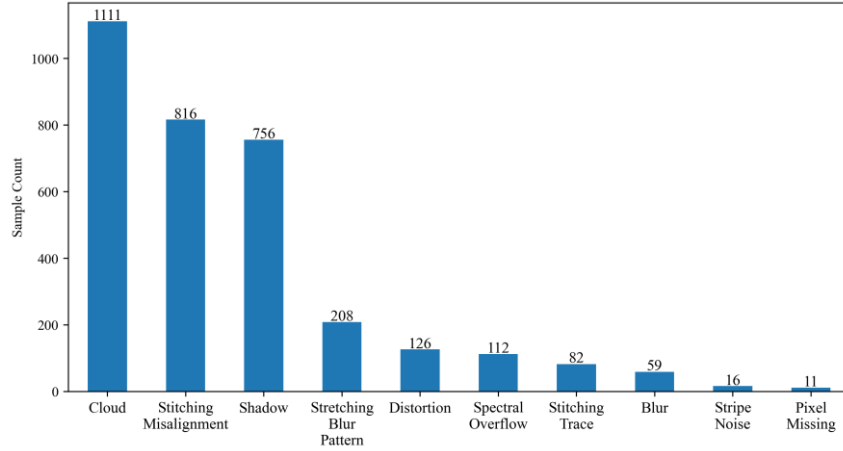


**Figure 3.** Statistics on the number of various samples in the dataset.

To address the issue of limited training data, the Stable Diffusion model [16], which has the ability to generate high-quality images based on textual guidance, is introduced in this study to augment data for the Stitching Trace and Spectral Overflow categories. A small set of remote sensing images (approximately 30) along with their corresponding textual descriptions are used to train the lora [17] model of the Stable Diffusion [16] method. Subsequently, this trained model is employed to generate a large number of similar images. This approach effectively expands the dataset, improves the performance of image classification, and is more efficient than manually generating data. The textual prompts used during training are in English, as shown in Table C1.

Because image generating is not completely controllable, it is necessary to manually filter the available images. We generate a total of 1000 samples first and manually select 200 of them, which could be used for image classification tasks. However, if they are to be used for semantic segmentation tasks, manually annotating masks would still be required, which is laborious. Therefore, the images generated by Stable Diffusion in this study are only applicable for image classification datasets.

### 3. Methods

The flowchart of the two-step detection system for remote sensing image quality inspection is shown in Figure 4, and each procedure in it will be introduced in detail in this section. In addition, we will introduce how we can explore the multimodal model.

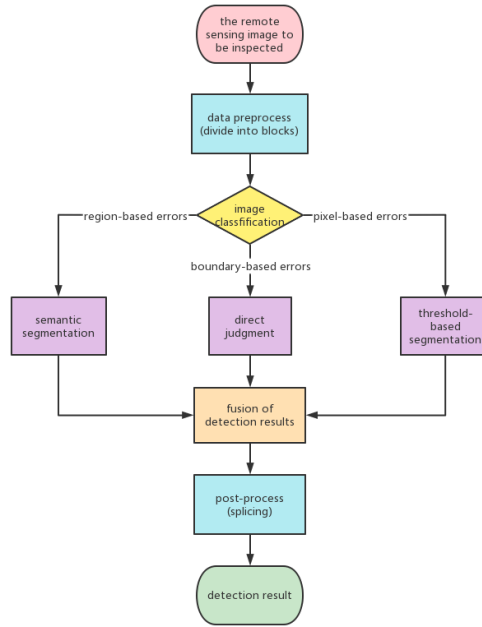


**Figure 4.** flowchart of the two-step detection system

### 3.1 Data Preprocessing and Post-processing

#### 3.1.1 Preprocessing

Since original remote sensing images are usually large and cannot be processed at once by deep learning models, we first divide them into smaller blocks. Unlike simple division, a specialized division strategy is proposed in this paper based on the characteristics of remote sensing image quality inspection, which has the following two features:

To avoid incomplete information and potential false negatives caused by a block containing an error region being divided into two blocks, the blocks in our method have overlapping areas between them. The width of the overlapping pixels between blocks is usually set to 1/5 of the image's side length.

Due to the significant differences in the actual area of the defective regions, such as "cloud" with actual widths ranging from tens of meters to tens of kilometers, it is difficult to detect both large and small area errors effectively by dividing the original image into fixed-size blocks. To address this issue, for the same image, we divide it into multiple sizes, typically using block sizes of 512x512 and 2048x2048 pixels, and performs a separate inspection for the entire image using different block sizes.

#### 3.1.2. Post-processing:

When merging and stitching the detection results of different blocks, conflicts may arise. A "conflict" refers to the situation where there are two or more different error types detected at the same position in the original image by different blocks. In case of a conflict, the region-based error will be determined based on the confidence score output by the semantic segmentation model. The priority order between 3 major error types is as follows: "pixel-based" errors first, followed by "region-based" errors, and finally "boundary-based" errors. Errors of high priority will override those of low priority.

Furthermore, to reduce noise in the results and avoid scattered and small detection areas, a dilation operation is performed on the binary mask corresponding to each error type in the semantic segmentation results. Then, connected components with an area smaller than a threshold (usually set to 0.01%) of the image area are discarded.

The concatenated mask, representing different error regions with different pixel values, is a single-channel image with the same size as the original remote sensing image. OpenCV is

used to perform contour detection on this mask, describing each error region as a polygon, and finally converting it into a shapefile.

### 3.2. Image Classification

Using semantic segmentation models directly can lead to a dilemma. Therefore, an intuitive approach is to perform an initial screening to eliminate certain options and avoid false detections. Since the dataset used in this paper is relatively balanced for image classification tasks (with approximately 30% of the samples being fully qualified images, which serve as negative samples, compared to 80% for semantic segmentation tasks, where negative samples represent background pixels), a good classification model can be obtained to provide correct constraints on the semantic segmentation model.

For image classification, the advanced Swin Transformer V2 model [18] is utilized in this paper to determine which small image blocks contain disqualified areas. This classification task involves multi-label binary classification, where each image is assessed for the presence of specific error types. The output dimension of the last classification layer is set to 10, with no changes made to the other parts of the model, which employs pre-trained weights. Given an input image, the model produces a 10-dimensional vector representing the logits for the 10 error types. Logits are the network's output values before any activation function is applied. The selected loss function is binary cross-entropy, as shown in equation (1), where  $\hat{y}$  represents the 10-dimensional network output vector and  $y$  denotes the true label, also a 10-dimensional vector with values of 1 or 0.  $C$  denotes the number of categories, here it is 10.  $y_c$  represents the  $c$ -th dimension of  $y$ .

$$Loss = -\frac{1}{C} \sum_{c=1}^C (\hat{y}_c \log \sigma(y_c) + (1 - \hat{y}_c) \log(1 - \sigma(y_c))) \quad (1)$$

When converting logits into classification results, a common threshold of 0.5 is applied. If the sigmoid activation value of a certain error type's logit exceeds 0.5, it is considered as present; otherwise, it is considered absent. If all logits are less than 0.5, the image is deemed fully qualified.

### 3.3 Three Major Class of Errors and Their Corresponding Specific Detection Methods

The 10 error types are classified into the following three major classes:

**Region-based errors:** Clouds, Shadows, Stretching Blur Patterns, Distortions, Blurs, and Spectral Overflow fall under this category. The nonconforming regions exhibit block-like shapes with a certain area. In quality inspection of remote sensing images, it is necessary to outline these regions and calculate their areas as a basis for deduction points. In this study, semantic segmentation methods are utilized for detection.

**Boundary-based errors:** Stitching Traces (also called color discrepancies) and Stitching Misalignments belong to this category. The nonconforming regions exhibit boundary-like patterns, often spanning several kilometers. To identify the boundary, a comparison between two adjacent regions within a larger visual range is required. In practical work, precise detection of the exact boundary location is not necessary, we only need to mark the approximate area where the boundary line is located. Therefore, image classification methods are sufficient to label such regions and the second processing step of such errors will not be evaluated or discussed separately. The detection effect of such errors will be reflected in the image classification procedure.

**Pixel-based errors:** Pixel Missing and Stripe Noise belong to this category. The nonconforming regions only occupy a few pixels, with extremely small areas. Semantic segmentation is not suitable for these cases due to their size. However, they possess distinct color characteristics, making them detectable using thresholding segmentation methods.

### 3.4. Handling Region-based Errors: Semantic Segmentation

For region-based errors, the shape of the areas is difficult to determine, and there is subjectivity in the segmentation process between "instances." It is challenging to precisely define the size of an "instance". Consequently, using instance segmentation or panorama segmentation can confuse the model during training. Instead, it is more natural to employ semantic segmentation models that do not require distinguishing instances.

We experiments with MobilenetV2 [19], Segformer [12], CLIPSeg [20], and GroupVit [21] models. Although models such as Mask2Former [22] and OneFormer [23] are more advanced in terms of performance, they are better suited for instance segmentation or panorama segmentation, and they have larger model sizes and slower training speeds. Therefore, they are not chosen in this study.

Since adding negative samples (fully qualified images) would result in an excessive number of background pixels in the training set, which negatively affects the performance of the semantic segmentation model, the semantic segmentation training set does not include negative samples. The loss function used to train MobilenetV2 [19] and Segformer [12] is the average of multi-class cross-entropy for all pixels, as shown in Equation 2, where  $K$  is the total number of pixels in one image,  $C$  is the number of categories,  $y_c^{(k)}$  is the predicted logit of  $k$ -th pixel of class  $c$  while  $\hat{y}_c^{(k)}$  is the binary label, and  $\sigma$  represents the *softmax* function. For CLIPSeg [20] training, the loss function is the average binary cross-entropy for all pixels in each binary mask, which can be seen as a special case where  $C = 2$  in Equation (2). GroupVit [21], on the other hand, does not require masks as labels but uses the textual description of the image as the label. The loss function for GroupVit [21] is contrastive loss, and further details can be found in the original paper [21].

$$Loss = -\frac{1}{K} \frac{1}{C} \sum_{k=1}^K \sum_{c=1}^C \hat{y}_c^{(k)} \log \sigma(y_c^{(k)}) \quad (2)$$

The segmentation results produced by the semantic segmentation model are adjusted based on the image classification results from the previous step to overcome the issue of high false detection rates. This will be discussed in detail in section 3.5.

### 3.5. Integration Methods of Image Classification and Semantic Segmentation

#### 3.5.1. Constraint at the Output Side

For the models having traditional semantic segmentation headers such as Segformer [12], the classification model constrains its output in three possible ways:

**Absolute constraint:** The output logits of the image classification model are simply converted into binary classification results. If an error category is not present, the corresponding pixels associated with that error type are discarded in the semantic segmentation results, i.e., set to 0. This method is advantageous in terms of convenience and computational speed. However, it can lead to error accumulation. If the image classification model provides incorrect predictions, even if the semantic segmentation is correct, those error types will be discarded, resulting in a high probability of missed detections.

**Relative constraint:** The logits of the corresponding error type in the semantic segmentation output are adjusted based on the confidence scores of each error type in the image classification results. Specifically, the logits of error type "a" in the semantic segmentation output are added to the logits of error type "a" in the image classification results. This method ensures that the results of image classification do not have an absolute influence and that the logits from both models are considered. However, changing the logits of certain categories may lead to unstable semantic segmentation results. For example, if the confidence score for "shadow" is high in image classification, it may result in nearly all pixels being classified as shadows in the semantic segmentation results.

**Intermediate constraint:** This method involves setting a threshold, typically 0.5. If the logits for error type "a" in the image classification results exceed the threshold, no adjustments are made to the logits in the semantic segmentation corresponding to that error type. Otherwise, the logits of error type "c" in the semantic segmentation output are added to the logits of error



type "c" in the image classification results after multiplied by a coefficient. This method offers the advantages of only lowering the confidence of categories with lower scores, while minimally affecting categories with high confidence scores. It mitigates the impact of image classification results on semantic segmentation and ensures that error types with low confidence in image classification are detected to some extent, reducing false detection rates.

These three constraint methods can be represented by one equation (3):

$$\hat{y}_s^{(c)} = \alpha y_c^{(c)} \epsilon(t - y_c^{(c)}) + y_s^{(c)} \quad (3)$$

$\alpha$  is a coefficient and  $t$  is a threshold (usually 0.5), which can be adjusted by users.  $\epsilon$  stands for Heaviside step function.  $y_c^{(c)}$  represents the logit of class  $c$  in the predicted results of the classification model.  $y_s^{(c)}$  represents the logit of class  $c$  of each pixel predicted by the segmentation model and  $\hat{y}_s^{(c)}$  is the corresponding adjusted logit. When  $\alpha$  approaches positive infinity and the threshold is set to 0, it corresponds to the absolute constraint. When the threshold approaches positive infinity and  $\alpha = 1$ , it corresponds to the Relative constraint. Setting other values can be seen as Intermediate constraint.

### 3.5.2. Constraint at the Input Side

For models such as CLIPSeg [20] and GroupVit [21], which are text-driven zero-shot semantic segmentation models, both the image and a list of  $n$  target object names to be detected are required as inputs. Therefore, the classification model provides constraints at the input side. The specific approach is as follows: First, the image classification results are transformed into  $n$  texts, where each text corresponds to the name of an error type classified as "yes." For example, if the "cloud" and "shadow" classes are classified as "yes" in the classification results, the input texts would be ["cloud", "shadow"]. These texts are then combined with the image and fed into the model. The model performs binary segmentation for each object mentioned in the input texts and does not perform segmentation for error types not present in the classification results, thereby avoiding false detections.

### 3.6. Handling Pixel-based Errors: Threshold-based Segmentation

For blocks identified as having pixel-based errors, semantic segmentation is not suitable due to their tiny size. However, these blocks exhibit distinct pixel values compared to the background. Therefore, we employ traditional image processing methods for discrimination.

Regions with Pixel missing typically have pixel values that are either all black or all white, and they may appear as individual pixels without any specific shape. To detect such regions, a threshold-based segmentation method is applied. Specifically, regions with pixel values of [0, 0, 0] or [255, 255, 255] are directly extracted as the detection results.

Stripe-like noise exhibits distinct shape characteristics, typically manifesting as short, thin lines that are noticeably different in color from the background. These lines are predominantly oriented horizontally or vertically, occasionally diagonally, but seldom appear as curves or jagged lines. Exploiting these shape and color features enables effective extraction of such noise. Typically, grayscale conversion is performed on images prior to binarization. However, this study reveals that in the grayscale images, stripe-like noise and the background may exhibit considerable similarity, while in a specific channel, the noise displays a distinct color contrast to the background. The results of binarization using the grayscale image and the red channel, along with the extracted stripe-like noise, are illustrated in Figure 5. It is evident from the figure that employing binarization on the red channel yields significantly superior detection results compared to binarizing the grayscale image.

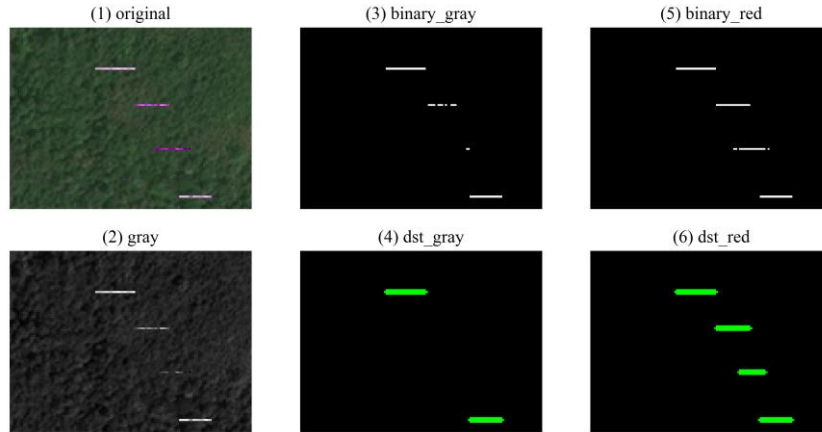


**Figure 5.** (1) Original image, (2) grayscale image, (3) grayscale image binarization, (4) result of extracting stripe noise by grayscale image binarization, (5) the red channel binarization, (6) result of extracting stripe noise by the red channel binarization

Hence, we employ the following approach for stripe-like noise detection: RGB channels are first separated, and Otsu binarization[24] is applied to each channel to detect connected components. Subsequently, the shape of all connected components is analyzed, and any component that appears as a rectangular region with an aspect ratio greater than 5 or less than 0.2 is identified as stripe-like noise. Finally, the union of the detection results of the three channels will be taken.

### 3.7. Exploration of Multimodal Models

In addition to traditional fixed-label image classification, the recently proposed image-text multimodal models can also be used for image classification. Although their classification accuracy may not be as high as dedicated classification models for specific tasks, they provide more comprehensive information and have greater versatility. They hold the potential for "one model for all tasks" and may be capable of addressing all image-related problems in remote sensing. Therefore, the application of multimodal models in the field of remote sensing is promising.

The structure of multimodal models is similar to generative language models, but with the addition of an image encoder that embeds the image as a vector alongside the textual prompt. The output of the model is identical to that of a language model. The training methodology for multimodal models is largely similar to language models and will not be elaborated upon in this paper.

A comparative experiment is conducted between BLIP [14], which possesses the ability to convert images into text, and VisualGLM [15], which supports long conversations. For BLIP [14], a Chinese pre-trained version is utilized, and the dataset mentioned in Section 2.2., consisting of images and their corresponding textual descriptions, is used for fine-tuning all parameters. As for the VisualGLM [15], due to its large size, a lora[17] training approach is employed. Only the layers with even numbers in the ChatGLM [15] part of VisualGLM [15] underwent lora training, while no modifications are made to other parts such as the image encoder. Subsequently, the Q&A dataset mentioned in Section 2.3. is used to train the model's ability to provide detailed descriptions of errors in remote sensing images.

## 4. Experiment Results

In this section, we first evaluate every individual process in the system, then the model integration method, and finally the multimodal model. Due to the large difference between the detection methods and goals of different error types, our system cannot be measured with a

single metric. Evaluation of the whole system will be reflected in the detection of different error types.

#### 4.1. Training Settings

All models are trained on a single NVIDIA GeForce RTX 3090 GPU using the AdamW optimizer. The learning rate scheduler is set to "cosine" with an initial learning rate of 1e-4. Table A1 contains the download links, parameter counts, the training input, label, test input, and output configurations for each pretrained model.

For all models except VisualGLM [15], random data augmentation is applied to the input images during training, including random horizontal and vertical flipping and random cropping on both images and their corresponding masks. Gaussian noise augmentation is not used to avoid affecting the model's detection.

For all image classification models, training is conducted for 10 epochs, while semantic segmentation models are trained for 5 epochs. In the case of Segformer [12], the background (qualified area) is treated as an additional class with label 0, and negative samples (images without errors) are excluded from the training set to avoid affecting the segmentation recall. The same approach is applied to CLIPSeg [20], where the background is also considered as a class. Correspondence between ID and label during models training is shown in Table 2.

**Table 2.** Correspondence between ID and label

ID	Labels of classification models	Labels of semantic segmentation models
0	Cloud	Background
1	Shadow	Cloud
2	Stretching Blur Pattern	Shadow
3	Blur	Stretching Blur Pattern
4	Spectral Overflow	Blur
5	Distortion	Spectral Overflow
6	Stitching Trace	Distortion
7	Stitching Misalignment	
8	Stripe Noise	
9	Pixel Missing	

For the multimodal model VisualGLM [15], lora training is employed with a lora rank of 16, focusing on the ChatGLM part and performing lora on layers [0,2,4,6,8,10,12,14,16,18,20,22,24,26] for 5 epochs. The Unet part of stable diffusion model is also trained using lora with a lora\_rank of 10 for 10 epochs.

#### 4.2. Results of Image Classification Models

ResNet [5] and SwinV2 [18] models are evaluated for image classification using accuracy, macro F1, and F1 scores per class. The text output from the image-to-text model BLIP [14] is mapped to labels in the same format as the classification model to be evaluated. For example, if BLIP [14] outputs "Satellite image with shadows and blur," it is mapped to the label [0,1,0,1,0,0,0,0,0].

Table 3 presents the experimental results for the classification task on the dataset. The accuracy represents the proportion of correctly classified samples for all 10 classes. The results demonstrate that the SwinV2 [18] model achieves better performance in remote sensing image quality classification, nearly achieving perfect classification for all classes, while ResNet [5] consistently performs weaker than other models. The BLIP [14] model also exhibits strong classification capabilities.

**Table 3.** Experimental results of various image classification models

Model	accuracy	macro F1	F1 per category
Resnet-50	0.9192	0.8491	[0.9719, 0.9701, 0.8947, 0.8125, 0.9734, 0.9600, 0.9600, 0.6000, 0.5000, 0.8500]
SwinV2-base	<b>0.9719</b>	<b>0.9827</b>	[0.9824, 0.9934, 0.9743, 1.0000, 0.8461, 1.0000, 1.0000, 0.9937, 1.0000, 0.9800]
BLIP	0.9670	0.9611	[0.9860, 0.9832, 0.9295, 0.9600, 0.9302, 1.0000, 0.8666, 0.9941, 1.0000, 0.9600]

Table 4 presents the impact of data augmentation on image classification models. The experimental results indicate that using the Stable Diffusion model for data augmentation further improves the performance of image classification and semantic segmentation, although it is not that much improvement.

**Table 4.** The effect of data augmentation

	macro F1 of SwinV2	macro F1 of BLIP
data augmentation	0.9780	0.9720
w/o data augmentation	0.9719	0.9611

#### 4.3. Results of Semantic Segmentation Models

Semantic segmentation is evaluated using the mean Intersection over Union (mIoU) metric and compared 4 segmentation models: Mobilenet-v2 [19], Segformer [12], CLIPSeg, and GroupVit [21]. The input for CLIPSeg [20] and GroupVit [21] during testing included both the test images and the names of existing error types in the images. Table 5 presents the mIoU scores and IoU scores for each class on the test dataset (these 7 categories are Background, Cloud, Shadow, Stretching Blur Pattern, Blur, Spectral Overflow and Distortion in order). The test dataset used in this case does not include negative samples.

**Table 5.** Experimental results of various semantic segmentation models

Model	mIoU	Per Category IoU
Mobilenet-v2	0.47153	[0.91771, 0.81417, 0.26575, 0.3878, 0.17978, 0.41014, 0.32538]
Segformer	<b>0.71266</b>	[0.95451, 0.86814, 0.65336, 0.48435, 0.90058, 0.76419, 0.36348]
CLIPSeg	0.40703	[0.93582, 0.84138, 0.359, 0.00941, 0.0000, 0.70027, 0.0033]
GroupVit	0.19406	[0.38743, 0.45659, 0.06993, 0.1379, 0.19186, 0.00175, 0.11297]

The results indicate that Segformer [12] outperforms other segmentation models in remote sensing image semantic segmentation tasks. However, the performance of text-driven models is poor, even when additional information, such as the names of existing error types in the images, is provided. This might be attributed to the need for extensive image-text data training for such models, while this study employed limited data and relatively homogeneous image categories. The results reveal that errors with explicit features such as clouds, shadows, blurriness, and spectral overflow are recognized with higher accuracy in the semantic segmentation task, while errors with more complex features like stretching blur pattern and distortions show relatively lower recognition accuracy.

#### 4.4. Detection of Pixel-based Errors

For pixel-based errors, which consist of only two types, IoU is calculated for these two error types. The results are shown in Table 6, demonstrating good detection performance. In addition, it is found in the experiment that appropriate saturation enhancement (in this experiment, the S channel value in HSV is increased by 100) can significantly improve the detection

result of stripe noise. However, since these types of errors are relatively scarce in the current test dataset, further verification is needed in the future to validate their effectiveness.

**Table 6.** Detection results of pixel-based errors

Detection Type	IoU
Stripe Noise Detection	0.4996
Stripe Noise Detection w/o saturation enhancement	0.3860
Pixel Missing Detection	0.9763

#### 4.5. Model Integration Method

To demonstrate the integration method of the two models, pixel precision and mIoU are used to evaluate the performance of semantic segmentation on region-level errors under different settings of parameter  $\alpha$  and  $t$ . The experimental results are shown in Table 7, which confirm that integrating two models significantly outperform using the semantic segmentation model alone (one-step), especially in terms of precision. When  $\alpha$  approaches infinity, indicating absolute priority given to the classification model, the overall performance is optimal, while setting  $\alpha$  to 0, equivalent to using a single model, leads to the poorest performance.

It can be clearly seen in Figure 6 that, for the image with large error area, two-step detection is almost consistent with one-step detection, proving that two-step detection, although more constrained, does not cause missing detection, and for images without error regions, the results of one-step detection contain a large amount of noises of misdetection, while two-step detection does not, demonstrating the high-precision of two-step detection.

It is worth noting that the negative samples in the test dataset only account for about 30%, which is much lower than the practical scenario, where our method will achieve more significant superiority in precision.

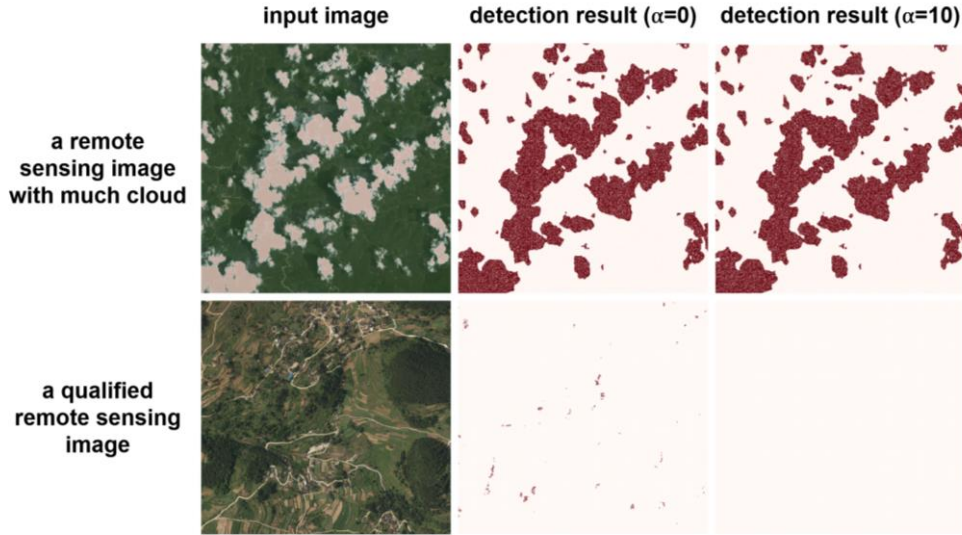


**Figure 6.** An image with cloud and a qualified image are tested at different values of  $\alpha$  and  $t = 0.5$ . In the detection result figure, the dark parts represent the detected errors and the light part represents eligibility.

**Table 7.** The influence of different values of  $a$  and  $t$  in equation (3).

$a$	$t$	mIoU	Pixel precision
0	0	0.6904	0.7880
100	0.5	<b>0.7124</b>	<b>0.8154</b>

1	0.5	0.7123	0.7985
0.3	0.9	0.7120	0.7981
0.1	0.5	0.6980	0.7831
0.3	0.01	0.7122	0.7984

#### 4.7. Evaluations of the Multimodal Model

The VisualGLM [15] model trained on image-based Q&As is evaluated on a test dataset consisting of 2000 question-answer pairs in the same format. Accuracy and Rouge scores are used for evaluation. Several Q&A examples in Figure 7 demonstrate the remote sensing image quality inspection capability of our fine-tuned multimodal model, proving the possibility of applying a universal model in this field.

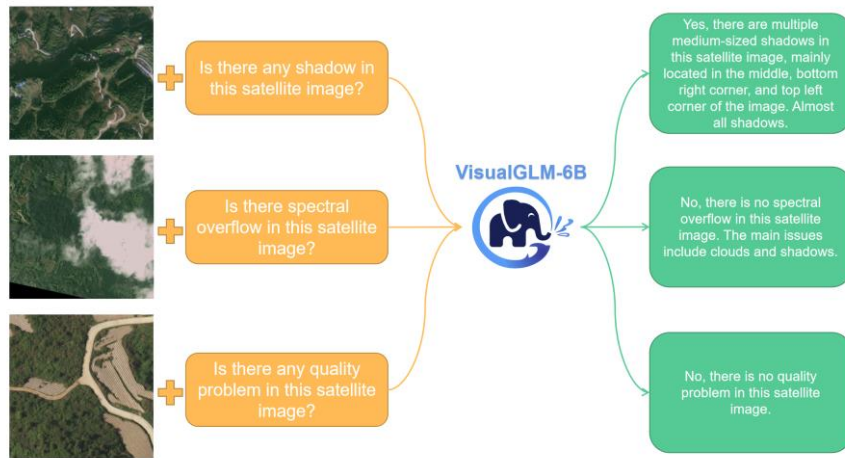


**Figure 7.** Some answers generated by VisualGLM based on remote sensing image quality inspection questions, which have been translated into English (Chinese Q&A for the actual trained model).

The evaluation results are presented in Table 8. Due to the relatively unpredictable outputs of the model, with answers that may be excessively long or not in the expected format, assessing classification accuracy directly becomes challenging, the accuracy metric is divided into two parts. The first part considers the model's output to be correct if it matches the label exactly, while the second part focuses only on binary classification, where the first character of the model's output ("yes" or "no") aligns with the label. The Rouge scores are divided into three parts, representing Rouge-1, Rouge-2, and Rouge-L evaluations. The result indicating that the fine-tuned VisualGLM [15] model can provide detailed descriptions of images. However, the accuracy is not competitive with classification models, and there are still cases where the answers do not correspond to the image content or fail to address the question, suggesting room for further improvement.

**Table 8.** Evaluation Results of VisualGLM

Model	accuracy (exact match)	accuracy (binary classification)	Rouge-1 f1	Rouge-2 f1	Rouge-l f1
VisualGLM	0.7144	0.8409	0.9000	0.8664	0.8847

## 5. Discussion

In this paper, our proposed two-step detection method, by combining image classification, semantic segmentation, and some image processing techniques, for the first time applies deep learning methods to the field of remote sensing image quality inspection, and achieves a 2.2% mIoU boost over the one-step detection method. This method takes about five minutes to detect an image at 10000 \* 10000 resolution on an entry-level graphics card with only 4GB memory, which is much more efficient and economical than humans.

For the image classification task, the SwinV2 [18] model outperforms the traditional ResNet [5] model by about 13% and BLIP [14] by about 2% on macro F1, making it the optimal choice for classifying the 10 types of error. However, the BLIP [14] model only has a slightly lower accuracy than SwinV2 [18], it offers better scalability and still deserves future research.

Regarding the semantic segmentation of region-based errors, Segformer [12] achieved the best performance, and when combined with the classification models, it further improved its precision. However, its classification method is relatively traditional and lacks strong scalability, making it suitable only for tasks with fixed categories. To achieve zero-shot capability, it is necessary to choose models like CLIPSeg [20] or GroupViT [21]. However, due to the limited quantity and single category of the training data for remote sensing image quality inspection, the current results of them are both poor, making it challenging to demonstrate their zero-shot capability and rich customization potential. This also validates that traditional semantic segmentation models still have advantages for a small amount of data with fixed classes.

For region-based error, by applying this method to practical work, we found that this method is more effective in detecting common errors such as Cloud and Shadow, while due to the complex features and small amount of data, the detection effect on Distortion and Stretching Blur Pattern is not ideal enough. In the future, it may be improved by further adding high-quality annotation data.

For boundary-based error, although the classification accuracy is very high in the test dataset, the misdetection (the qualified area is judged as error) often occurs in our practical work, which may be because the patterns of these error types in the dataset are homogeneous. More different styles of such errors will be needed in the future work.

For pixel-based error, our proposed threshold-based segmentation method achieves rather good results. However, due to the small amount of test dataset, its validity still needs to be further proved in practical work.

The multimodal large model VisualGLM [15], although demonstrating some error detection capability, falls short in terms of stable and accurate classification compared to the classification models. This can be attributed to three main reasons: First, remote sensing image quality inspection falls into a specialized domain rather than common knowledge, and the pretraining of large models lacks expertise in this specific field, resulting in insufficient understanding of both images and text with jargons. Second, compared to the large model's pretraining dataset, the dataset used in this study is limited in quantity. Third, VisualGLM [15] is based on the ChatGLM [15] language model, with only 6 billion parameters, making it challenging to achieve the same level of answer quality as models like GPT-4, which has over 175 billion parameters. The good news is there is ample room for improvement, such as employing thought chain prompts by multiple rounds of dialogue and incorporating external knowledge by designing questions with auxiliary information or by embedding a knowledge graph. A real example of incorporating external knowledge is: give VisualGLM [15] a remote sensing image with "spectral overflow" and ask "Is there any spectral overflow in this image?" The model will give the wrong answer of "No". If you add "spectral overflow refers to some red, yellow, blue and green patches in the remote sensing image" to the question, the model will give the correct answer of "spectral overflow does exist in this image". Due to time and data limitations in this study, a more in-depth investigation in this regard is not conducted. Nevertheless, it must be acknowledged that general multimodal large models possess great potential and are worth exploring in future research.

## 6. Conclusion

This paper proposed a two-step remote sensing image quality inspection system based on deep learning techniques, aiming to address the inefficiency of traditional methods. The results of this research remained favorable even in challenging conditions such as multi-cloud and rugged terrain in Guizhou remote sensing images, indicating the potential applicability to images from various regions. This study is significant for improving the efficiency and accuracy of remote sensing image quality inspection, providing valuable insights for research and applications in the field of remote sensing image processing as well as other areas of remote sensing.

Future work can explore advanced vision models and attempt to incorporate more remote sensing image data into the dataset to improve the model's generalization and robustness. Additionally, training a multimodal general-purpose model that combines images, texts and other information can be pursued to further enhance the capabilities of remote sensing image processing in the zero-shot manner. Furthermore, applying this method to real-world remote sensing image processing scenarios for wider validation and practical applications should be considered.

**Author Contributions:** Y.Y is responsible for concepts and experiments, C.L. and H.W is responsible for data annotation, and T.W. and K.R is responsible for coordinating the entire project.

**Data Availability Statement:** The remote sensing image quality inspection dataset, trained models and code are all available on Tsinghua Cloud Disk (<https://cloud.tsinghua.edu.cn/d/7b3167ee4b8d4242a8d1/>).



## Appendix A

The models used in this article, their download links, parameter amount, input and output, are shown in Table A1.

**Table A1.** The models used in this paper

Task	Model	Download address	Params	Input (Training/Testing)	Labels (Training/Testing)
Image classification	Resnet-50	<a href="https://huggingface.co/microsoft/resnet-50">https://huggingface.co/microsoft/resnet-50</a>	25M	Image/Image	Multi-label binary classification vector/ Multi-label binary classification vector
	SwinV2-base	<a href="https://huggingface.co/microsoft/swinv2-base-patch4-window12-192-224">https://huggingface.co/microsoft/swinv2-base-patch4-window12-192-224</a>	104M	Image/Image	Multi-label binary classification vector/ Multi-label binary classification vector
Image-text multi-modality	BLIP-Chinese	<a href="https://huggingface.co/IDEA-CCNL/Taiyi-BLIP-750M-Chinese">https://huggingface.co/IDEA-CCNL/Taiyi-BLIP-750M-Chinese</a>	750M	Image/Image	A textual description of Image/ A textual description of Image
	VisualGLM	<a href="https://huggingface.co/THUDM/VisualGLM-6b">https://huggingface.co/THUDM/VisualGLM-6b</a>	6B	Image and question/ Image and question	Textual answer/ Textual answer
Semantic segmentation	Mobilenet-v2	<a href="https://huggingface.co/google/mobilenet_v2_1.0_224">https://huggingface.co/google/mobilenet_v2_1.0_224</a>	2.6M	Image/Image	Multivariate Mask/ Multivariate Mask
	Segformer-b5	<a href="https://huggingface.co/nvidia/segformer-b5-finetuned-ade-640-640">https://huggingface.co/nvidia/segformer-b5-finetuned-ade-640-640</a>	80M	Image/Image	Multivariate Mask/ Multivariate Mask
Zero-shot semantic segmentation	CLIPSeg	<a href="https://huggingface.co/CIDAS/CLIPSeg-rd64-refined">https://huggingface.co/CIDAS/CLIPSeg-rd64-refined</a>	144M	Image and Object Name/ Image and Object Name*n	Binary Mask/ Binary Mask*n
	groupvit	<a href="https://huggingface.co/nvidia">https://huggingface.co/nvidia</a>	53M	Image*n, A textual description of	Contrastive learning, no explicit labels/

		<a href="https://github.com/google-research/google-research/blob/master/groupvit_gcc_yfcc">a/groupvit-gcc-yfcc</a>		Image *n/ Image and Object Name*n	Multivariate Mask
Text to image	stable-diffusion-v1-5	<a href="https://huggingface.co/runwayml/stable-diffusion-v1-5">https://huggingface.co/runwayml/stable-diffusion-v1-5</a>	1B	A textual description of Image/ A textual description of Image	Image/ Image

## Appendix B

When the multimodal model is trained, the correspondence between the image content and the corresponding template for text Q&A is shown in Table B1. All QAs are in Chinese. If the number of connected fields in a binary image corresponding to an error is equal to 1, the text is described as "一处", and if it is greater than 1, the text is described as "多处". Table B2, Table B3 and Figure B1 respectively shows how the area size, the type of the boundary line and the position of the error region are described as text.

**Table B1.** The image content with the corresponding template for text Q&A.

Model	Task objectives	Errors present in the Image	question	answer
BLIP	image classification	any	无	卫星图像中存在{错误名 1, 错误名 2...}。
		non-existent	无	卫星图像完全合格。
VisualGLM	image classification	any	这张卫星图像是否存在质量问题？	是，这张卫星图像有质量问题，问题类型有：{错误名 1, 错误名 2...}。
		non-existent	这张卫星图像是否存在质量问题？	否，这张卫星图像没有质量问题。
	Region-based errors	这张卫星图像中是否存在{错误名}？	是，这张卫星图像中存在{一/多}处{大/中等/小/微小}面积的{错误名}，主要位于图像的{位置}。	
	detailed description	Boundary-based errors	这张卫星图像中是否存在{错误名}？	是，这张卫星图像中存在一条{错误名}的痕迹，位于图像的{位置}，大致是{横线/竖线/斜线/折线}。
		pixel-based errors	这张卫星图像中是否存在{错误名}？	是，这张卫星图像中存在{一/多}处{错误名}，主要位于图像的{位置}。

**Table B2.** The proportion of area corresponds to the Chinese text description

$0.4 < a \leq 1$	$0.1 < a \leq 0.4$	$0.01 < a \leq 0.1$	$0.0001 < a \leq 0.01$	$0 \leq a \leq 0.0001$
大	中等	小	微小	不存在

**Table B3.** The angle  $\theta$  between the line and the x-axis corresponds to the Chinese text description

$0^\circ < \theta < 30$	$60 < \theta < 90$	$30 < \theta < 60$	Not a straight line
横线	竖线	斜线	折线



**Figure B1.** The main location of an error is defined as the location of the centroid of the largest connected component in the Binary image representing such errors. Divide an image into 9 grids, corresponding to 9 different position descriptions in Chinese, so that the model can roughly locate and describe errors.

## Appendix C

**Table C1.** Correspondence between text prompt and the image content used in Stable Diffusion training.

Text Prompt	Image Content
"Red, yellow, green, or blue patches in satellite images."	Image with Spectral Overflow
"Color difference between two parts of Satellite imagery."	Image with Stitching Trace

## References

- [1] Z. Zhu and C. E. Woodcock, "Object-based cloud and cloud shadow detection in Landsat imagery," *Remote Sensing of Environment*, vol. 118, pp. 83–94, Mar. 2012, doi: 10.1016/j.rse.2011.10.028.
- [2] I. Kotaridis and M. Lazaridou, "Remote sensing image segmentation advances: A meta-analysis," *ISPRS Journal of Photogrammetry and Remote Sensing*, vol. 173, pp. 309–322, Mar. 2021, doi: 10.1016/j.isprsjprs.2021.01.020.
- [3] Y. Lecun, L. Bottou, Y. Bengio, and P. Haffner, "Gradient-based learning applied to document recognition," *Proceedings of the IEEE*, vol. 86, no. 11, pp. 2278–2324, Nov. 1998, doi: 10.1109/5.726791.
- [4] A. Krizhevsky, I. Sutskever, and G. E. Hinton, "ImageNet classification with deep convolutional neural networks," *Commun. ACM*, vol. 60, no. 6, pp. 84–90, May 2017, doi: 10.1145/3065386.
- [5] K. He, X. Zhang, S. Ren, and J. Sun, "Deep Residual Learning for Image Recognition," arXiv, arXiv:1512.03385, Dec. 2015. doi: 10.48550/arXiv.1512.03385.
- [6] F. Iandola, M. Moskewicz, S. Karayev, R. Girshick, T. Darrell, and K. Keutzer, "DenseNet: Implementing Efficient ConvNet Descriptor Pyramids," arXiv, arXiv:1404.1869, Apr. 2014. doi: 10.48550/arXiv.1404.1869.

- [7] A. G. Howard *et al.*, "MobileNets: Efficient Convolutional Neural Networks for Mobile Vision Applications." arXiv, Apr. 16, 2017. doi: 10.48550/arXiv.1704.04861.
- [8] J. Long, E. Shelhamer, and T. Darrell, "Fully Convolutional Networks for Semantic Segmentation," presented at the Proceedings of the IEEE Conference on Computer Vision and Pattern Recognition, 2015, pp. 3431–3440. Accessed: Jun. 02, 2023. [Online]. Available: [https://openaccess.thecvf.com/content\\_cvpr\\_2015/html/Long\\_Fully\\_Convolutional\\_Networks\\_2015\\_CVPR\\_paper.html](https://openaccess.thecvf.com/content_cvpr_2015/html/Long_Fully_Convolutional_Networks_2015_CVPR_paper.html)
- [9] O. Ronneberger, P. Fischer, and T. Brox, "U-Net: Convolutional Networks for Biomedical Image Segmentation." arXiv, May 18, 2015. Accessed: Jun. 02, 2023. [Online]. Available: <http://arxiv.org/abs/1505.04597>
- [10] A. Vaswani *et al.*, "Attention is All you Need," in *Advances in Neural Information Processing Systems*, I. Guyon, U. V. Luxburg, S. Bengio, H. Wallach, R. Fergus, S. Vishwanathan, and R. Garnett, Eds., Curran Associates, Inc., 2017. [Online]. Available: [https://proceedings.neurips.cc/paper\\_files/paper/2017/file/3f5ee243547dee91fbd053c1c4a845aa-Paper.pdf](https://proceedings.neurips.cc/paper_files/paper/2017/file/3f5ee243547dee91fbd053c1c4a845aa-Paper.pdf)
- [11] Z. Liu *et al.*, "Swin Transformer: Hierarchical Vision Transformer using Shifted Windows." arXiv, Aug. 17, 2021. Accessed: Apr. 25, 2023. [Online]. Available: <http://arxiv.org/abs/2103.14030>
- [12] E. Xie, W. Wang, Z. Yu, A. Anandkumar, J. M. Alvarez, and P. Luo, "SegFormer: Simple and Efficient Design for Semantic Segmentation with Transformers," in *Advances in Neural Information Processing Systems*, Curran Associates, Inc., 2021, pp. 12077–12090. Accessed: May 21, 2023. [Online]. Available: <https://proceedings.neurips.cc/paper/2021/hash/64f1f27bf1b4ec22924fd0acb550c235-Abstract.html>
- [13] OpenAI, "GPT-4 Technical Report," arXiv, arXiv:2303.08774, Mar. 2023. doi: 10.48550/arXiv.2303.08774.
- [14] J. Li, D. Li, C. Xiong, and S. Hoi, "BLIP: Bootstrapping Language-Image Pre-training for Unified Vision-Language Understanding and Generation," in *Proceedings of the 39th International Conference on Machine Learning*, PMLR, Jun. 2022, pp. 12888–12900. Accessed: May 21, 2023. [Online]. Available: <https://proceedings.mlr.press/v162/li22n.html>
- [15] Z. Du *et al.*, "GLM: General Language Model Pretraining with Autoregressive Blank Infilling." arXiv, Mar. 17, 2022. doi: 10.48550/arXiv.2103.10360.
- [16] R. Rombach, A. Blattmann, D. Lorenz, P. Esser, and B. Ommer, "High-Resolution Image Synthesis with Latent Diffusion Models." arXiv, Apr. 13, 2022. Accessed: May 22, 2023. [Online]. Available: <http://arxiv.org/abs/2112.10752>
- [17] E. J. Hu *et al.*, "LoRA: Low-Rank Adaptation of Large Language Models." arXiv, Oct. 16, 2021. Accessed: Feb. 10, 2023. [Online]. Available: <http://arxiv.org/abs/2106.09685>
- [18] Z. Liu *et al.*, "Swin Transformer V2: Scaling Up Capacity and Resolution." arXiv, Apr. 11, 2022. doi: 10.48550/arXiv.2111.09883.
- [19] M. Sandler, A. Howard, M. Zhu, A. Zhmoginov, and L.-C. Chen, "MobileNetV2: Inverted Residuals and Linear Bottlenecks." arXiv, Mar. 21, 2019. doi: 10.48550/arXiv.1801.04381.
- [20] T. Lüddecke and A. S. Ecker, "Image Segmentation Using Text and Image Prompts." arXiv, Mar. 30, 2022. doi: 10.48550/arXiv.2112.10003.
- [21] J. Xu *et al.*, "GroupViT: Semantic Segmentation Emerges from Text Supervision." arXiv, Jul. 18, 2022. doi: 10.48550/arXiv.2202.11094.

- [22] B. Cheng, I. Misra, A. G. Schwing, A. Kirillov, and R. Girdhar, "Masked-attention Mask Transformer for Universal Image Segmentation," arXiv, arXiv:2112.01527, Jun. 2022. doi: 10.48550/arXiv.2112.01527.
- [23] J. Jain, J. Li, M. Chiu, A. Hassani, N. Orlov, and H. Shi, "OneFormer: One Transformer to Rule Universal Image Segmentation." arXiv, Dec. 26, 2022. doi: 10.48550/arXiv.2211.06220.
- [24] N. Otsu, "A Threshold Selection Method from Gray-Level Histograms," *IEEE Transactions on Systems, Man, and Cybernetics*, vol. 9, no. 1, pp. 62–66, Jan. 1979, doi: 10.1109/TSMC.1979.4310076.